EWHT-AIB: Enhanced Waist-mounted Human Tracking Framework Based on Array IMU and Barometer

Feifan Lin, Qingzhong Cai*, *Senior Member*, *IEEE*, Yue Yu*, and Huizheng Yuan

***Abstract*—With the development of the Internet of Things (IoT) and Artificial Intelligence (AI), indoor location-based services have become an indispensable part of public daily life. The performance of 3D indoor positioning is constrained by the low performance of consumer-grade MEMS IMU, lack of effective calibration for barometer, and the poor adaptability to complex human motion modes. To address above challenges, this paper proposes an enhanced waist-mounted human tracking framework based on array IMU and barometer (EWHT-AIB) that combines array IMU data fusion, precise barometer calibration, and motion-constrained position-attitude update algorithm to achieve robust and accurate indoor positioning. To enhance array IMU data fusion performance, a weighted data fusion algorithm for array IMU based on the bias instability coefficients is proposed to achieve effective weighted fusion of array IMU data. Subsequently, a barometer calibration algorithm based on nonlinear fitting is proposed to achieve accurate compensation for bias error and scale factor error of the barometer. Finally, a position-attitude update algorithm under motion constraints is designed to achieve accurate pedestrian 3D indoor positioning using compensated array IMU and barometer data. Comprehensive experiments demonstrate that the proposed EWHT-AIB framework can achieve meter-level positioning accuracy under typical indoor environments.**

***Index Terms*—Indoor localization, Array IMU data fusion, Barometer calibration, Motion constraints , Sensor fusion.**

I. INTRODUCTION

With the advent of the ubiquitous navigation era and the rapid development of wearable devices, there is an increasing demand for accessing personal location information anytime and anywhere, as well as for receiving services based on this information. Positioning and navigation systems integrate sensing, communication, and Internet of Things (IoT) technologies to deliver reliable location data [1]. While the Global Navigation Satellite System (GNSS) is a dependable method for positioning in outdoor open areas, its signals can be disrupted in environments such as indoor spaces, rendering it ineffective [2]. Consequently, achieving accurate indoor positioning in GNSS-denied environments remains a significant challenge.

To provide location-based services in GNSS-denied indoor environments, various positioning technologies utilizing external information sources have been developed, including Wi-Fi [3], Bluetooth [4], ultra-wideband (UWB) [5], and radio frequency infrared devices [6]. However, due to the complexity and variability of indoor spaces, positioning methods that depend on external infrastructure incur high costs, and wireless signal positioning base stations are vulnerable to interference and damage [7]. Pedestrian positioning technology based on MEMS IMU autonomously collects inertial data using the MEMS IMU and calculates positioning results through inertial navigation algorithms without requiring additional positioning signals [8]. This capability allows for inertial positioning in any location scenario.

Currently, indoor human tracking based on MEMS IMU can be broadly categorized into three types: waist-mounted MEMS IMU-based tracking [9], foot-mounted MEMS IMU-based tracking [10], and leg-mounted MEMS IMU-based tracking [11]. Among these, waist-mounted systems are more suitable for accurate indoor human tracking due to their ease of wear and distinctive data features. Waist-mounted MEMS IMU-based tracking technologies primarily include gait detection, stride length estimation, orientation estimation, and position computation [9]. Yu et al. [12] proposed a high-precision positioning method based on multi-feature fusion using a body-worn inertial sensor network, where inertial nodes mounted on the waist, shank, and foot are fused in a weighted manner to estimate the yaw angle. However, due to the limited accuracy of individual nodes, the yaw angle still tends to drift rapidly over time. Hajati et al. [13] introduced a pedestrian localization device mounted on a belt, which utilizes both IMUs and barometers to compute the three-dimensional position of the pedestrian, though the method lacks effective calibration of barometric sensor errors. Pham et al. [14] proposed a smoothing algorithm based on constrained optimization to estimate stride length from a waist-mounted IMU under the assumption of a known total walking distance. However, this method struggles to maintain performance under mixed gait conditions.

Therefore, at the current stage, achieving an autonomous and accurate indoor three-dimensional positioning system

This manuscript was submitted June 04, 2025 to the IEEE Transactions on Instrumentation and Measurement for review. This work was supported by the National Natural Science Foundation of China under Grants 62473028. (*Corresponding authors: Qingzhong Cai; Yue Yu.*)

Feifan Lin, Qingzhong Cai are with the School of Instrumentation and Optoelectronic Engineering, Beihang University, Beijing 100191, China (e-mail: feifan_lin@buaa.edu.cn; qingzhong_cai@buaa.edu.cn).

Yue Yu is with the Department of Land Surveying and Geo-Informatics, the Hong Kong Polytechnic University, Hongkong 999077, China (e-mail: michael-yue.yu@polyu.edu.hk).

Huizheng Yuan is with the School of Mechanical Engineering, Hubei University of Technology, Wuhan 430000, China (e-mail: huizhengyuan@163.com).

requires addressing the following challenges:

1. Rapid error drift of a single IMU: The pedestrian positioning method based on a waist-mounted MEMS IMU can only maintain positioning accuracy for a short period due to the rapid divergence of sensor biases [15]. The array IMU technology, by fusing data from multiple low-precision MEMS IMU, can effectively suppress the random noise of MEMS IMU, improving the data output accuracy of MEMS IMU and ultimately enhancing the positioning accuracy of the system [16]. Data fusion algorithms play a crucial role in the final performance improvement of the array IMU. Wang et al. [17] proposed improving the positioning performance of the array IMU through precise calibration. They first calibrated an array of 16 IMUs and then applied a traditional mean fusion algorithm to the fused data. Subsequently, a vehicle dynamic combined positioning experiment was conducted, and the results showed that the positioning accuracy of the calibrated array IMU system was 3.4 times that of a single IMU. Xing et al. [18] combined high-cost, short-range MEMS gyroscopes with low-cost, long-range MEMS gyroscopes and proposed an adaptive data fusion method suitable for redundant MEMS gyroscopes, which expands the angular rate measurement range while saving IMU configuration costs and volume. XUE et al. [19] proposed a data fusion algorithm based on a MEMS gyroscope array, where the angle random walk of the virtual gyroscope was reduced by approximately 4.86 times.

2. Deterministic error calibration of the barometer: In indoor environments, IMU-based human tracking frameworks can only provide two-dimensional position estimates [20]. Therefore, they are often combined with barometers to enable 3D indoor pedestrian localization. Qin et al. [21] integrated Zero-Velocity Update (ZUPT) with barometric readings to enhance the accuracy of height estimation. Wang et al. [22] further improved indoor pedestrian height estimation by combining barometric data with a height constraint algorithm based on 3D building models. Li et al. [23] fused barometric measurements with floor detection using cross-sectional analysis to achieve more reliable height estimation. Cong et al. [24] proposed a hybrid height estimation algorithm that balances high accuracy and practicality, thereby improving the precision of vertical localization in indoor settings. However, all of the above methods lack effective calibration for the deterministic errors of the barometer.

3. Human tracking under mixed gait motion conditions: In indoor human tracking based on waist-mounted MEMS IMU, maintaining high-precision localization under mixed gait conditions presents a significant challenge. Tran et al. [25] proposed a novel multi-model long short-term memory network to learn temporal features of mixed gait patterns; however, this method requires substantial computational resources and is unsuitable for deployment on lightweight embedded systems. Bhongade et al. [26] introduced a gait classifier based on support vector machines, which similarly demands considerable computational power, making real-time execution on small-scale embedded platforms difficult.

Aiming at the above problems and challenges, this paper proposes an enhanced waist-mounted human tracking framework based on array IMU and barometer (EWHT-AIB). The contributions of this work are summarized as follows:

1) To improve the data fusion accuracy of array IMU, this paper develops a weighted data fusion algorithm for array IMU based on the bias instability coefficient. Compared with a single IMU, the noise coefficient of the sensor of the weighted data fusion array IMU can be reduced by about 0.9 times, which is close to the theoretical limit value.
2) This paper proposes an effective barometer calibration algorithm based on nonlinear fitting. Experimental results from multi-floor tests show that the relative altitude error of the calibrated barometer can be reduced from 0.33 m to 0.05 m.
3) To achieve accurate indoor 3D positioning, this paper develops a position-attitude update algorithm under motion constraints that effectively integrates data from an array IMU and a barometer to enable precise indoor 3D positioning. Complex indoor experiments demonstrate that the proposed algorithm can achieve meter-level 3D positioning accuracy.

The structure of the remaining sections of this article is organized as follows. Section II introduces the array IMU data fusion algorithm based on bias instability coefficients, barometer calibration algorithm based on nonlinear fitting, and position-attitude update algorithm under motion constraints. Section III presents the experimental results of the presented EWHT-AIB. Section IV summarizes the whole paper and indicates the future work.

II. Research Methodology

Fig. 1 illustrates the overall structure of the proposed EWHT-AIB framework, which composed of three primary components: the array IMU data fusion module, the barometer calibration module, and the position-attitude update module under motion constraints.

A. Array IMU data fusion algorithm based on bias instability coefficients

Existing studies indicate that precise error calibration is essential for improving the accuracy of array IMU data fusion [17]. Therefore, before fusion, we calibrate each IMU in the array to eliminate systematic sensor errors. The calibration models for the accelerometer and gyroscope are defined as follows [17] :

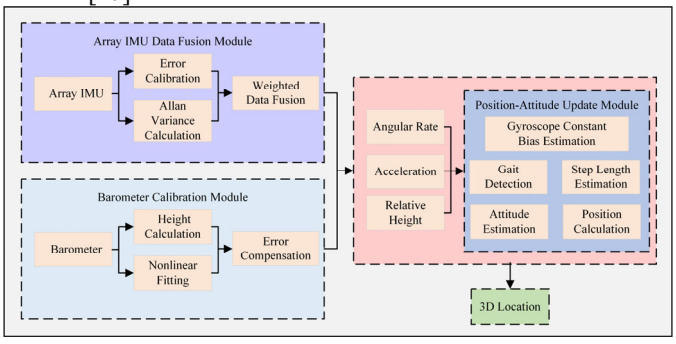

Fig. 1. Structure of Proposed EWHT-AIB Framework.

$$\begin{cases} \boldsymbol{A}_i = \boldsymbol{a}_{i0} + \boldsymbol{K}_i \boldsymbol{a}_i \\ \boldsymbol{\omega}_i = \boldsymbol{w}_{i0} + \boldsymbol{S}_i \boldsymbol{w}_i \end{cases} \tag{1}$$

where $\boldsymbol{A}_i$ is the measurement vector of the i-th triaxial accelerometer; $\boldsymbol{a}_i$ denotes the corresponding true acceleration vector; $\boldsymbol{a}_{i0}$ is the constant bias vector; $\boldsymbol{K}_i$ is the calibration matrix for the accelerometer; similarly, $\boldsymbol{\omega}_i$ represents the measurement vector of the i-th triaxial gyroscope; $\boldsymbol{w}_i$ denotes the corresponding true angular velocity vector; $\boldsymbol{w}_{i0}$ is the constant bias vector; $\boldsymbol{S}_i$ is the calibration matrix for the gyroscope.

Based on these calibration models, the IMUs are calibrated using the multi-position [27] and multi-rate method [28] to correct systematic errors. The weighted data fusion model for the array IMU is then defined as follows:

$$\begin{cases} \boldsymbol{w} = \sum_{n=1}^{4} \boldsymbol{k}_{gyro\_n} \boldsymbol{w}_{gyro\_n}, & n = 1,2,3,4 \\ \boldsymbol{a} = \sum_{n=1}^{4} \boldsymbol{k}_{acc\_n} \boldsymbol{a}_{acc\_n}, & n = 1,2,3,4 \end{cases} \tag{2}$$

where $\boldsymbol{w}$ is the fused angular rate vector obtained via weighted averaging; $\boldsymbol{w}_{gyro\_n}$ denotes the angular rate vector measured by the gyroscope of the n-th IMU; $\boldsymbol{k}_{gyro\_n}$ is the corresponding weight matrix derived from the bias instability coefficients. similarly, $\boldsymbol{a}$ is the fused accelerometer output; $\boldsymbol{a}_{acc\_n}$ is the acceleration output of the n-th IMU, and $\boldsymbol{k}_{acc\_n}$ is its weight matrix based on bias instability coefficients.

The weight allocation matrix for the gyroscope is computed based on its axis-specific bias instability coefficients derived from Allan variance analysis. The resulting matrix is defined as follows:

$$\boldsymbol{k}_{gyro\_n} = \mathrm{diag}\left(\frac{1/B_{gx,n}}{\sum_{n=1}^{4} 1/B_{gx,n}}, \frac{1/B_{gy,n}}{\sum_{n=1}^{4} 1/B_{gy,n}}, \frac{1/B_{gz,n}}{\sum_{n=1}^{4} 1/B_{gz,n}} \right), \quad n = 1,2,3,4 \tag{3}$$

where $B_{gx,n}$, $B_{gy,n}$ and $B_{gz,n}$ are the bias instability coefficients for the X, Y, and Z axes of the n-th IMU's gyroscope.

The weight allocation matrix for accelerometer is as follows:

$$\boldsymbol{k}_{acc\_n} = \mathrm{diag}\left(\frac{1/B_{ax,n}}{\sum_{n=1}^{4} 1/B_{ax,n}}, \frac{1/B_{ay,n}}{\sum_{n=1}^{4} 1/B_{ay,n}}, \frac{1/B_{az,n}}{\sum_{n=1}^{4} 1/B_{az,n}} \right), \quad n = 1,2,3,4 \tag{4}$$

where $B_{ax,n}$, $B_{ay,n}$ and $B_{az,n}$ denote the bias instability coefficients of the X, Y, and Z axes of the n-th IMU's accelerometer, respectively.

To clearly illustrate the process of array IMU data fusion, Fig. 2. depicts the complete workflow from error calibration to weighted fusion. This strategy improves the robustness of inertial fusion by mitigating sensor drift and enhancing pose estimation accuracy.

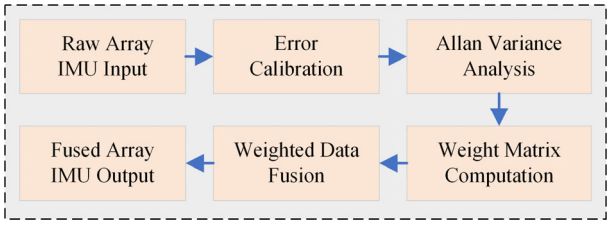

Fig. 2. Workflow of the array IMU data fusion.

B. Barometer calibration algorithm based on nonlinear fitting

Indoor vertical positioning is achieved by estimating inter-floor height differences using barometric pressure readings. The corresponding barometric altitude is computed from atmospheric pressure as follows [29]:

$$h_a = 44330 \cdot \left(1.0 - \left(\frac{100p}{p_0}\right)^{\frac{1.0}{5.255}}\right) \tag{5}$$

where h_a is the estimated barometric altitude, p is the measured air pressure, and P_0 is the standard sea-level reference pressure.

However, barometric altitude is highly sensitive to environmental changes such as temperature and humidity, which can lead to significant drift and errors over time. To address this, relative altitude is used instead of absolute altitude for indoor vertical positioning. The relative barometric height is calculated as follows:

$$h_r(i) = h_a(i) - h_b \tag{6}$$

where $h_r(i)$ is the relative height at the time i, $h_a(i)$ denotes the barometric altitude measured at time i, h_b refers to the initial barometric altitude recorded at the start of the positioning session.

To mitigate nonlinear distortions and residual bias in the barometer output, a nonlinear calibration model is introduced. The corrected relative height is calculated as follows:

$$h_{rc}(i) = k_2 \cdot h_r^2(i) + k_1 \cdot h_r(i) + k_0 \tag{7}$$

where $h_{rc}(i)$ is the corrected relative height at time i, k_2, k_1 and k_0 are calibration coefficients obtained via curve fitting.

To address barometric drift and nonlinear distortion, a calibration process based on nonlinear fitting is employed, as shown in Fig. 3. Atmospheric pressure is first converted to altitude, from which relative height is derived. A quadratic model then corrects residual bias, enabling meter-level vertical accuracy and supporting robust 3D pedestrian localization in multistory indoor environments.

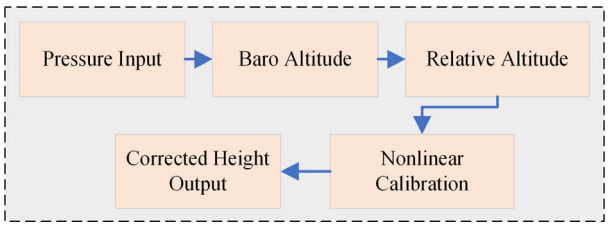

Fig. 3. Workflow of the barometric height calibration.

C. Position-attitude update algorithm based on motion constraints

1）Gyroscope Constant Bias Estimation Based on Modulus Variance Constraint

Accurate attitude estimation requires compensating the gyroscope's bias. This subsection presents a simple variance-based estimation method.

Specifically, the modulus of the three-axis gyroscope output at time *k* is defined as:

$$\omega_{\mathrm{mod},k}=\sqrt{\omega_{x,k}^2+\omega_{y,k}^2+\omega_{z,k}^2} \tag{8}$$

where $\omega_{x,k}$, $\omega_{y,k}$ and $\omega_{z,k}$ denote the angular rates along the *x*-, *y*-, and *z*-axes at time *k*, and $\omega_{\mathrm{mod},k}$ indicates the overall angular rate magnitude.

To identify potential static periods, the system evaluates the temporal stability of the angular rate by computing the variance of the modulus within a sliding buffer of size *N*. The variance is calculated as follows:

$$\sigma_{\omega,k}^2=\frac{1}{N}\sum_{i=k-N+1}^{k}\left(\omega_{\mathrm{mod},i}-\bar{\omega}_{\mathrm{mod},k}\right)^2 \tag{9}$$

where $\sigma_{\omega,k}^2$ is the variance of the angular rate modulus within the buffer, and $\bar{\omega}_{\mathrm{mod},k}$ denotes the mean value of the modulus over the buffer.

A static condition is considered detected when the variance falls below a predefined threshold, expressed as:

$$\sigma_{\mathrm{mod},k}^2<\sigma_{\mathrm{th}}^2 \tag{10}$$

where σ_{th}^2 is the variance threshold for static detection.

Upon detection of a static period, the constant bias of the three-axis gyroscope is estimated by averaging the corresponding gyroscope measurements accumulated during the static state. The bias estimates at time *k* are given by:

$$\begin{cases} b_{x,k}=\sum_{i=1}^{n_k} q_{x,i}\,/\,n_k \\ b_{y,k}=\sum_{i=1}^{n_k} q_{y,i}\,/\,n_k \\ b_{z,k}=\sum_{i=1}^{n_k} q_{z,i}\,/\,n_k \end{cases} \tag{11}$$

where $b_{x,k}$, $b_{y,k}$ and $b_{z,k}$ denote the estimated constant biases along the *x*-, *y*-, and *z*-axes, respectively; n_k is the number of static samples accumulated up to time *k*; and $q_{x,i}$, $q_{y,i}$ and $q_{z,i}$ are the corresponding static outputs of the three-axis gyroscope.

2）Gait Detection Based on Multi-Condition Constraints

Pedestrian gait detection relies on analyzing the variation in the norm of the accelerometer output within each gait cycle. The accelerometer norm is computed as follows:

$$Acc_{norm}=\sqrt{a_x^2+a_y^2+a_z^2} \tag{12}$$

where a_x, a_y and a_z are the calibrated output of the triaxial accelerometer; Acc_{norm} is the norm of the accelerometer output.

Previous studies have detected pedestrian gait by applying threshold-based peak and trough detection on the accelerometer norm [30]. However, due to body sway and noise during walking, false peaks and troughs may appear in the accelerometer norm signal, resulting in erroneous or missed gait event detections. To address this, this paper proposes a pedestrian gait detection method based on multiple condition constraints. By enforcing gait cycle consistency and step frequency constraints, the method effectively eliminates false peaks and troughs, thereby improving detection accuracy.

Taking normal walking gait detection as an example, the peak and trough thresholds of the accelerometer norm are empirically determined to distinguish valid steps from background noise. For the current subject, the typical values are as follows:

$$\begin{cases} Acc_{norm\_wp} = 10.8\ m/s^2 \\ Acc_{norm\_wt} = 8.8\ m/s^2 \end{cases} \tag{13}$$

where Acc_{norm_wp} and Acc_{norm_wt} are the respective thresholds for peak and trough detection during walking.

A complete gait cycle must include one peak and one trough in the accelerometer norm, occurring consecutively. Thus, peaks and troughs violating this gait cycle pattern are discarded.

After removing false peaks and troughs inconsistent with gait cycle characteristics, further pruning is performed based on step frequency constraints. The step frequency constraint during walking is expressed as follows:

$$f_{\mathrm{walk}}>\delta_{\mathrm{walk}} \tag{14}$$

where f_{walk} is the step frequency of pedestrian walking; δ_{walk} is the threshold for step frequency constraint during pedestrian walking. $\delta_{\mathrm{walk}}=120$ can be set for a pedestrian's walking.

The algorithm flowchart for walking gait detection is shown in the Fig. 4.

For upstairs and downstairs gait detection, the initial step is to determine the trend of the barometer's relative altitude output under the current pedestrian motion state. This identifies whether the pedestrian is ascending or descending stairs. Subsequently, the accelerometer data is used to count the number of steps during stair climbing or descending.

Considering that the height of a single stair step in the experimental setup is 0.15 m, the constraint condition for recognizing upstairs/downstairs mode is formulated as:

$$\Delta d=\mid d_n-d_1\mid>D_{\mathrm{step}} \tag{15}$$

where Δd denotes the absolute change in relative altitude measured by the barometer during stair navigation, d_1 and d_n represent the last and first values in the relative altitude buffer, respectively, and D_{step} corresponds to the step height. The buffer size n for storing relative altitude measurements is adjusted according to the application scenario. In our

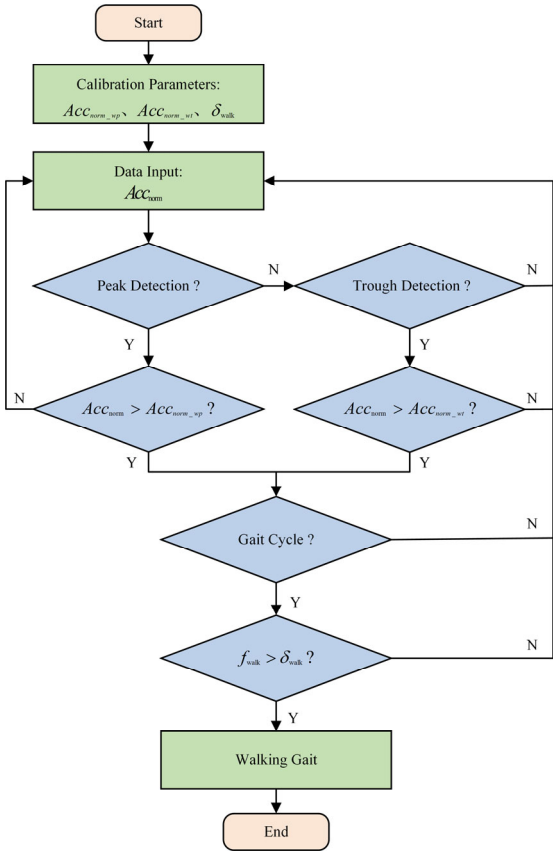

Fig. 4. Flowchart of the walking gait detection algorithm.

experiment, the barometer sampling frequency is set to 50 Hz, and a typical step-up/down action for a 0.15 m stair step is observed to take approximately 0.5 seconds. Therefore, n is set to 25 to ensure sufficient temporal coverage. This value may need to be adjusted under different stair heights, motion speeds, or use cases.

Upon completion of the height constraint verification, the upstairs and downstairs gait detection continues by following the workflow outlined in Fig. 4. This approach ensures that step detection and validation processes are consistently applied during stair navigation, facilitating accurate identification of gait events in these contexts.

3) Step Length Estimation Based on Gait Classification

The most commonly used pedestrian step length estimation method is as follows [30]:

$$L = J\sqrt[4]{A_{\text{peak}} - A_{\text{trough}}} \tag{16}$$

where L is the estimated step length; J is the step length coefficient used for correction; A_{peak} and A_{trough} are the peak and trough of the accelerometer norm within the gait cycle.

Building upon the previously described accurate gait detection, this study achieves precise step length estimation by classifying gait types and pre-calibrating the corresponding step length coefficients. For instance, the calibration formula for the walking step length coefficient is given by:

$$J_{\text{walk}} = S_{\text{walk\_gt}} / \sum_{i=1}^{N} L_{i\_\text{walk}} \tag{17}$$

where J_{walk} is the walking step length coefficient; $S_{\text{walk\_gt}}$ is the actual walking distance used for calibration; L_{i_walk} is the step length of the i-th step during calibration; and N is the total number of steps taken during calibration.

Since step length varies among pedestrians and gait types, coefficients must be pre-calibrated for each gait. During movement, accurate step length estimation is achieved by applying the corresponding calibrated coefficient for the detected gait type.

4) Attitude Estimation Based on QEKF and Step Yaw Constraint

To estimate pedestrian attitude in 3D space, we adopt a Quaternion-based Extended Kalman Filter (QEKF) framework [31]. The initial attitude angles are computed as follows:

$$\begin{cases} \theta_0 = \text{asin}(a_{y,0} / \sqrt{a_{x,0}^2 + a_{y,0}^2 + a_{z,0}^2}) \\ \phi_0 = \text{atan2}(-a_{x,0} / a_{z,0}) \\ \psi_0 = 0 \end{cases} \tag{18}$$

where θ_0, ϕ_0, ψ_0 denote the initial pitch, roll, and yaw angles respectively; $a_{x,0}$, $a_{y,0}$ and $a_{z,0}$ represent the triaxial accelerometer measurements at the initial time.

The pedestrian attitude estimation state vector is initialized as follows:

$$\boldsymbol{X}(0) = [q_0(0)\ q_1(0)\ q_2(0)\ q_3(0)\ b_{gx}(0)\ b_{gy}(0)\ b_{gz}(0)]^{\text{T}} \tag{19}$$

where $\boldsymbol{X}(0)$ is the initial state vector; $q_0(0)$, $q_1(0)$, $q_2(0)$ and $q_3(0)$ form the initial quaternion representing the pedestrian's attitude, $b_{gx}(0)$, $b_{gy}(0)$ and $b_{gz}(0)$ denote the initial gyroscope biases, all initialized to zero.

The state equation for pedestrian attitude estimation is as follows:

$$\boldsymbol{X}(k) = \begin{bmatrix} (\text{I}_{4\times4} + t(\boldsymbol{\Omega}_b(k)/2))\boldsymbol{q}(k-1) \\ \boldsymbol{b}_g(k-1) \end{bmatrix} + \begin{bmatrix} \boldsymbol{W}_q(k-1) \\ \boldsymbol{W}_g(k-1) \end{bmatrix} \tag{20}$$

where $\boldsymbol{q}(k-1)$ is the column vector composed of the quaternion representing the pedestrian's attitude at time k-1; $\boldsymbol{b}_g(k-1)$ is the random drift vector of the triaxial gyroscope at time k-1; $\boldsymbol{W}_q(k-1)$ and $\boldsymbol{W}_g(k-1)$ constitute the system noise matrix at time k-1; t is the sampling time interval; $\boldsymbol{\Omega}_b(k)/2$ is the coefficient matrix of the quaternion differential equation at time k.

The expanded form of $\boldsymbol{\Omega}_b(k)$ is as follows:

$$\boldsymbol{\Omega}_b(k) = \begin{bmatrix} 0 & -\hat{\omega}_x(k) & -\hat{\omega}_y(k) & -\hat{\omega}_z(k) \\ \hat{\omega}_x(k) & 0 & \hat{\omega}_z(k) & -\hat{\omega}_y(k) \\ \hat{\omega}_y(k) & -\hat{\omega}_z(k) & 0 & \hat{\omega}_x(k) \\ \hat{\omega}_z(k) & \hat{\omega}_y(k) & -\hat{\omega}_x(k) & 0 \end{bmatrix} \tag{21}$$

where $\hat{\omega}_x(k)$, $\hat{\omega}_y(k)$, and $\hat{\omega}_z(k)$ are the estimated values of the angular rate outputs from the triaxial gyroscope at time k.

The relationship between the estimated and measured values of the gyroscope at time k is as follows:

$$\begin{bmatrix}\hat{\omega}_x(k)\\ \hat{\omega}_y(k)\\ \hat{\omega}_z(k)\end{bmatrix}=\begin{bmatrix}\omega_x(k)\\ \omega_y(k)\\ \omega_z(k)\end{bmatrix}-\begin{bmatrix}b_{x,k}\\ b_{y,k}\\ b_{z,k}\end{bmatrix}-\begin{bmatrix}0\\ \omega_{ey}(k-1)\\ \omega_{ez}(k-1)\end{bmatrix} \tag{22}$$

where $\omega_x(k)$, $\omega_y(k)$, and $\omega_z(k)$ are the measured values of the angular rate outputs from the triaxial gyroscope at time k; $\omega_{ex}(k-1)$ and $\omega_{ey}(k-1)$ are the components of the earth's rotational angular velocity at time k-1 on the X-axis and Y-axis of the gyroscope.

The state one-step prediction matrix for pedestrian attitude estimation at time k is as follows [32]:

$$\hat{\boldsymbol{X}}(k,k-1)=\boldsymbol{\Phi}(k,k-1)\hat{\boldsymbol{X}}(k-1) \tag{23}$$

where $\hat{\boldsymbol{X}}(k,k-1)$ is the state one-step prediction matrix at time k; $\boldsymbol{\Phi}(k,k-1)$ is the state one-step transition matrix at time k; $\hat{\boldsymbol{X}}(k-1)$ is the state estimation matrix at time k-1.

The state one-step transition matrix at time k is expanded as follows:

$$\boldsymbol{\Phi}(k,k-1)=\begin{bmatrix}1 & \frac{-t\hat{\omega}_x(k)}{2} & \frac{-t\hat{\omega}_y(k)}{2} & \frac{-t\hat{\omega}_z(k)}{2} & \frac{tq_1(k-1)}{2} & \frac{tq_2(k-1)}{2} & \frac{tq_3(k-1)}{2}\\ \frac{t\hat{\omega}_x(k)}{2} & 1 & \frac{t\hat{\omega}_z(k)}{2} & \frac{-t\hat{\omega}_y(k)}{2} & \frac{-tq_0(k-1)}{2} & \frac{tq_3(k-1)}{2} & \frac{-tq_2(k-1)}{2}\\ \frac{t\hat{\omega}_y(k)}{2} & \frac{-t\hat{\omega}_z(k)}{2} & 1 & \frac{t\hat{\omega}_x(k)}{2} & \frac{-tq_3(k-1)}{2} & \frac{-tq_0(k-1)}{2} & \frac{tq_1(k-1)}{2}\\ \frac{t\hat{\omega}_z(k)}{2} & \frac{t\hat{\omega}_y(k)}{2} & \frac{-t\hat{\omega}_x(k)}{2} & 1 & \frac{tq_2(k-1)}{2} & \frac{-tq_1(k-1)}{2} & \frac{-tq_0(k-1)}{2}\\ 0 & 0 & 0 & 0 & 1 & 0 & 0\\ 0 & 0 & 0 & 0 & 0 & 1 & 0\\ 0 & 0 & 0 & 0 & 0 & 0 & 1\end{bmatrix} \tag{24}$$

The state one-step prediction mean squared error matrix for pedestrian attitude estimation at time k is as follows [33]:

$$\boldsymbol{P}(k,k-1)=\boldsymbol{\Phi}(k,k-1)\boldsymbol{P}(k-1)\boldsymbol{\Phi}^{\mathrm{T}}(k,k-1)+\boldsymbol{Q}(k-1) \tag{25}$$

where $\boldsymbol{P}(k,k-1)$ is the state one-step prediction mean squared error matrix at time k; $\boldsymbol{P}(k-1)$ is the state estimation mean squared error matrix at time k-1; $\boldsymbol{Q}(k-1)$ is the covariance matrix of the system noise matrix at time k-1.

The observation vector for pedestrian attitude estimation at time k is as follows:

$$\boldsymbol{Z}(k)=[a_x(k)\ \ a_y(k)\ \ a_z(k)]^{\mathrm{T}} \tag{26}$$

where $\boldsymbol{Z}(k)$ is the observation vector at time k; $a_x(k)$, $a_y(k)$, and $a_z(k)$ are the measurements of the triaxial accelerometer at time k.

The observation equation for pedestrian attitude estimation at time k is as follows:

$$\boldsymbol{Z}(k)=\begin{bmatrix}2g(q_1(k)q_3(k)-q_0(k)q_2(k))\\ 2g(q_2(k)q_3(k)+q_0(k)q_1(k))\\ g(q_0^2(k)-q_1^2(k)-q_2^2(k)+q_3^2(k))\end{bmatrix}+\boldsymbol{v}(k) \tag{27}$$

where g is the local gravitational acceleration; $\boldsymbol{v}(k)$ is the measurement noise matrix at time k.

The filtering gain matrix for pedestrian attitude estimation at time k is as follows [34]:

$$\boldsymbol{K}(k)=\boldsymbol{P}(k,k-1)\boldsymbol{H}^{\mathrm{T}}(k)[\boldsymbol{H}(k)\boldsymbol{P}(k,k-1)\boldsymbol{H}^{\mathrm{T}}(k)+\boldsymbol{R}(k)]^{-1} \tag{28}$$

where $\boldsymbol{K}(k)$ is the filtering gain matrix at time k; $\boldsymbol{H}(k)$ is the measurement matrix at time k; $\boldsymbol{R}(k)$ is the covariance matrix of the measurement noise matrix at time k.

The measurement matrix at time k is expanded as follows:

$$\boldsymbol{H}(k)=\begin{bmatrix}-2gq_2(k) & 2gq_3(k) & -2gq_0(k) & 2gq_1(k) & 0 & 0 & 0\\ 2gq_1(k) & 2gq_0(k) & 2gq_3(k) & 2gq_2(k) & 0 & 0 & 0\\ 2gq_0(k) & -2gq_1(k) & -2gq_2(k) & 2gq_3(k) & 0 & 0 & 0\end{bmatrix} \tag{29}$$

The estimated state vector for pedestrian attitude estimation at time k is as follows:

$$\hat{\boldsymbol{X}}(k)=\hat{\boldsymbol{X}}(k,k-1)+\boldsymbol{K}(k)[\boldsymbol{Z}(k)-\boldsymbol{H}(k)\hat{\boldsymbol{X}}(k,k-1)] \tag{30}$$

where $\hat{\boldsymbol{X}}(k)$ is the estimated state vector at time k.

The state estimation mean square error matrix for pedestrian attitude estimation at time k is as follows:

$$\boldsymbol{P}(k)=[\mathrm{I}-\boldsymbol{K}(k)\boldsymbol{H}(k)]\boldsymbol{P}(k,k-1) \tag{31}$$

where $\boldsymbol{P}(k)$ is the state estimation mean square error matrix at time k.

The pedestrian attitude angles at time k are as follows:

$$\begin{cases}\theta_k=\mathrm{atan2}[2q_0(k)q_2(k)-2q_1(k)q_3(k),\\ \qquad q_0^2(k)-q_1^2(k)-q_2^2(k)+q_3^2(k)]\\ \phi_k=\mathrm{atan2}[2q_0(k)q_3(k)-2q_1(k)q_2(k),\\ \qquad q_0^2(k)-q_1^2(k)+q_2^2(k)-q_3^2(k)]\\ \psi_k=\mathrm{asin}[2q_2(k)q_3(k)+2q_0(k)q_1(k)]\end{cases} \tag{32}$$

where θ_k, ϕ_k, and ψ_k are the pitch, roll, and yaw of the pedestrian at time k.

When pedestrians walk along a straight line, small yaw perturbations occur due to body sway, while the overall direction remains unchanged. To enhance yaw accuracy, these perturbations must be constrained.

The step yaw is defined as the yaw estimated at gait detection. To limit linear motion yaw errors, a step yaw buffer is constructed:

$$\boldsymbol{\psi}_{\mathrm{buf}}=[\psi_0,\psi_1,\psi_2] \tag{33}$$

where $\boldsymbol{\psi}_{\mathrm{buf}}$ is the step yaw buffer, considering that yaw constraint should not cause excessive time delays, the buffer size is chosen to be 3; ψ_0, ψ_1, and ψ_2 are the three consecutive step yaws stored in the step yaw buffer.

The maximum change in step yaw within the current step yaw buffer is calculated as follows:

$$\Delta\psi=\max(\boldsymbol{\psi}_{\mathrm{buf}})-\min(\boldsymbol{\psi}_{\mathrm{buf}}) \tag{34}$$

$\Delta\psi$ is the maximum difference among the three consecutive step yaws of the pedestrian, this difference is used to determine whether the pedestrian is in a state of linear motion, with the specific determination criteria as follows:

$$\begin{cases}\Delta\psi\geq 5, \text{ turning state}\\ \Delta\psi<5, \text{ linear motion state}\end{cases} \tag{35}$$

5) 3D Position Calculation

The pedestrian's 3D position after walking k steps is calculated as follows:

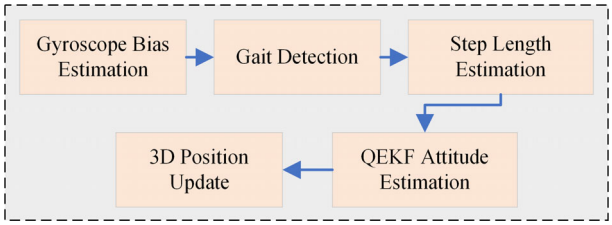

Fig. 5. Workflow of the position and attitude update algorithm.

Fig. 6. EWHT-AIB test system setup.

$$\begin{cases} x_k = x_0 + \sum_{i=1}^{k} L_i \cos\psi_i \\ y_k = y_0 + \sum_{i=1}^{k} L_i \cos\psi_i \\ z_k = h_0 + h_{rc}(k) \end{cases} \tag{36}$$

where x_k, y_k and z_k denote the 3D position coordinates after k steps; x_0, y_0 and z_0 represent the initial position coordinates, typically initialized to zero; L_i is the step length of the i-th step; ψ_i is the walking heading angle of the i-th step relative to the navigation coordinate system's X-axis; $h_{rc}(k)$ is the calibrated relative height from the barometer after k steps.

In summary, this study addresses three key challenges in indoor 3D localization through a unified data fusion framework. First, a bias-instability-weighted array IMU fusion method improves inertial measurement accuracy. Second, a nonlinear barometer calibration algorithm corrects altitude drift for vertical estimation. Finally, a motion-constrained position-attitude update algorithm, as illustrated in Fig. 5, combines gait detection, step estimation, and QEKF-based attitude filtering to achieve robust 3D pedestrian localization.

III. Experimental Results of EWHT-AIB

This section presents a series of experiments conducted in a typical indoor environment to evaluate the performance of the proposed EWHT-AIB system. To establish a clear correspondence between system design and overall performance, we independently assess the core functional modules, including the array IMU fusion algorithm, the barometer calibration method, and the position-attitude update algorithm. Subsequently, a comprehensive evaluation of the integrated EWHT-AIB framework is performed. The experimental setup is shown in Fig. 6, and the main technical specifications of the array IMU and barometer are listed in TABLE I and TABLE II.

TABLE I
THE MAIN TECHNICAL CHARACTERISTICS OF ARRAY IMU

Indexes	Gyroscope	Accelerometer
Sampling rate	200 Hz	200 Hz
Dynamic range	±500 °s^{-1}	±10 g
Nonlinearity	±0.2 %FS	±0.5 %FS
Initial offset	±1 °s^{-1}	±50 mg

TABLE II
THE MAIN TECHNICAL CHARACTERISTICS OF BAROMETER

Indexes	Barometer
Sampling rate	50 Hz
Pressure measurement range	10 ~ 1200 mbar
Altitude measurement accuracy	10 cm
Pressure conversion time	1 ms

A. Performance evaluation of array IMU data fusion algorithm

To improve the accuracy of inertial measurements, this study introduces a weighted data fusion algorithm for array IMUs, where fusion weights are determined by the bias instability coefficients of individual sensors. To validate its effectiveness, an eight-hour static test was conducted using a fully calibrated array IMU, and Allan variance analysis was performed to quantify noise characteristics.

Fig. 7 and Fig. 8 compare the Allan variance curves of the Z-axis gyroscope and accelerometer before and after applying the proposed algorithm. Compared to the conventional mean fusion method, the weighted fusion significantly suppresses noise fluctuations and yields smoother Allan profiles.

TABLE III summarizes the quantitative comparison. The results show that the proposed method reduces the Z-axis noise coefficient by approximately 0.9 times, clearly demonstrating its superiority over the traditional approach in enhancing data fusion accuracy.

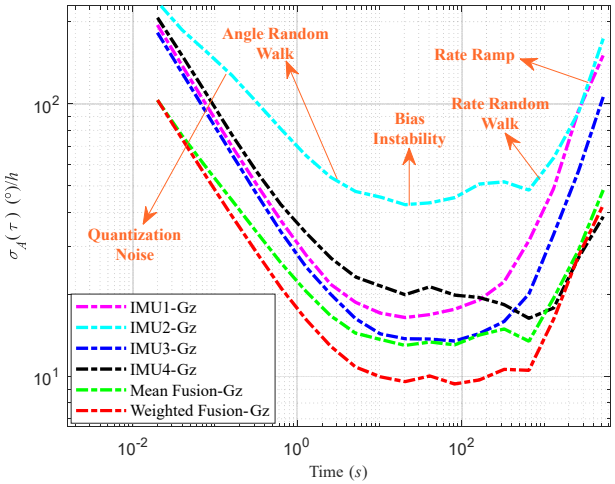

Fig. 7. Gyroscope Allan variance comparison.

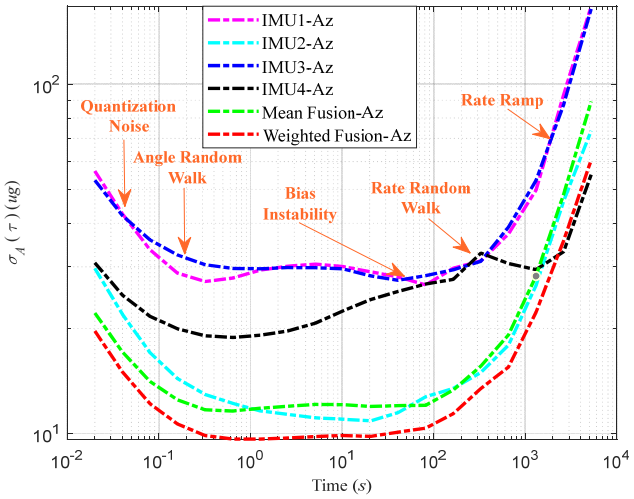

Fig. 8. Accelerometer Allan variance comparison.

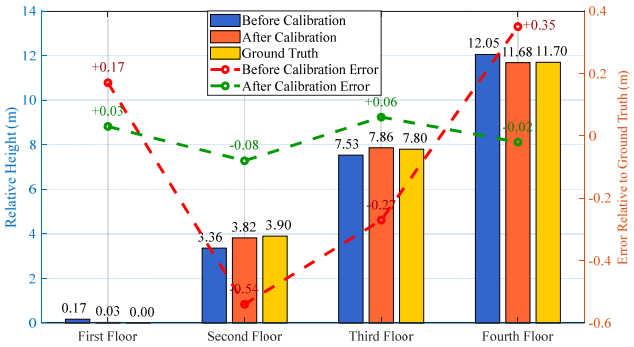

Fig. 9. Comparison of the output relative height before and after barometer calibration.

TABLE III
ARRAY IMU Z-AXIS NOISE PERFORMANCE REDUCTION TIMES

Methods	GyrBI	GyrRW	AccBI	AccRW
Mean Fusion	0.87	0.80	0.85	0.83
This paper	0.97	0.90	0.95	0.92

B. Performance evaluation of barometer calibration algorithm

To address the vertical drift and limited accuracy of barometric measurements, this study introduces a nonlinear fitting-based calibration algorithm aimed at correcting systematic errors in the barometer's relative altitude output. The calibration procedure involves collecting pressure-derived height data across multiple indoor floors and fitting a nonlinear correction model to refine the barometer's response.

As illustrated in Fig. 9, the raw and calibrated relative altitude outputs are compared across four floor transitions. The calibrated results exhibit significantly improved consistency with true floor heights. Quantitatively, the mean error in barometric height estimation is reduced from 0.33 m to 0.05 m, clearly demonstrating the effectiveness of the proposed calibration approach.

By substantially enhancing vertical accuracy, this module ensures reliable altitude information for downstream fusion with inertial data, thereby improving the overall robustness of the EWHT-AIB positioning system.

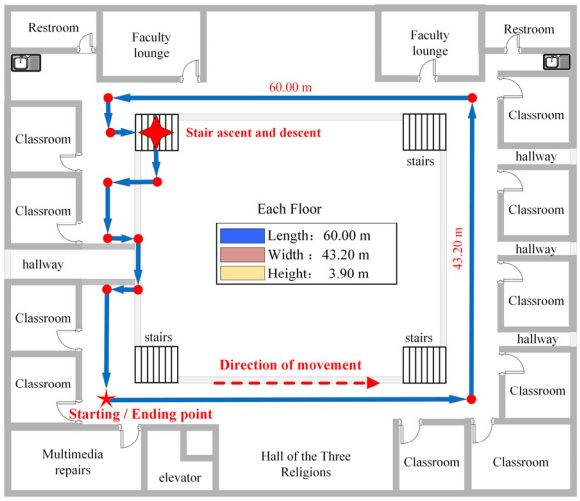

Fig. 10. 2D floor plan of the positioning experiment route.

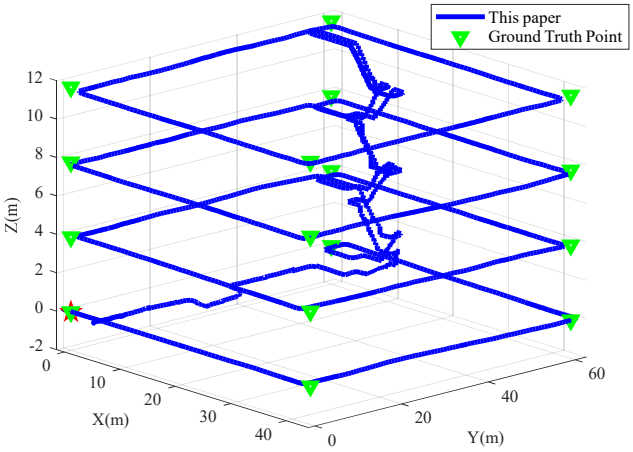

Fig. 11. 3D trajectory map of the positioning experiment.

C. Performance evaluation of position-attitude update algorithm

To achieve accurate indoor 3D pedestrian localization, this study proposes a position-attitude update algorithm that fuses array IMU and barometer data under motion constraints. To validate its effectiveness, a series of experiments were conducted in a typical indoor multistory environment.

The experimental site comprises a four-story building with each floor measuring 60.00 m in length, 43.20 m in width, and 3.90 m in height. The test route, illustrated in Fig. 10, covers a total path length of 1 km with a 15-minute duration, during which the participant performs various activities including walking, stair ascent, and descent.

Fig. 11 presents the 3D trajectory obtained by the proposed algorithm. The blue curve denotes the estimated trajectory, the red pentagram marks the starting point, and green triangle markers represent manually measured ground-truth points at each floor corner, which serve as reference locations for positioning error evaluation.

To further analyze positioning performance, Fig. 12 presents the cumulative distribution function (CDF) of horizontal localization errors, which indicates the probability that the positioning error is below a certain threshold. The 75th percentile error, marked with dotted vertical lines and numerical annotations, reflects the threshold below which 75%

of the horizontal errors fall—a widely adopted metric for performance evaluation. As shown, the proposed method achieves a 75th percentile horizontal error of 2.51 m, significantly outperforming the traditional pedestrian dead reckoning (PDR) algorithm, which exhibits a corresponding error of 14.23 m. This comparison highlights the substantial accuracy improvement provided by our approach.

Similarly, Fig. 13 illustrates the CDF of vertical positioning errors before and after barometer calibration and motion-constrained fusion. The 75th percentile vertical error is reduced to 0.15 m after applying our method, compared to 0.40 m using the uncalibrated barometer. This result confirms that our algorithm effectively enhances vertical localization accuracy, particularly under floor-changing or stair-climbing scenarios where elevation precision is critical.

Fig. 14 compares the horizontal positioning accuracy of the array IMU versus a single IMU. Results from five repeated trials show that the array IMU achieves an average horizontal error of 2.60 m, whereas the single IMU reaches 4.90 m, indicating that the proposed array fusion strategy improves horizontal positioning accuracy by approximately 47%.

Finally, the consistency of performance across five experiments is summarized in TABLE IV, where the proposed position-attitude update algorithm achieves a mean horizontal error of 2.61 m and a mean altitude error of 0.15 m, reaffirming its robustness and accuracy.

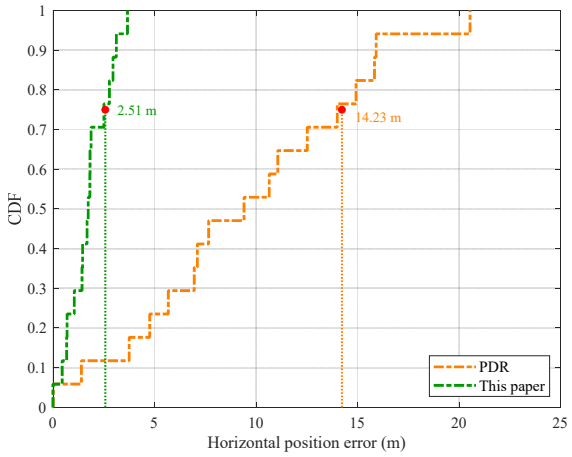

Fig. 12. Horizontal error CDF curve.

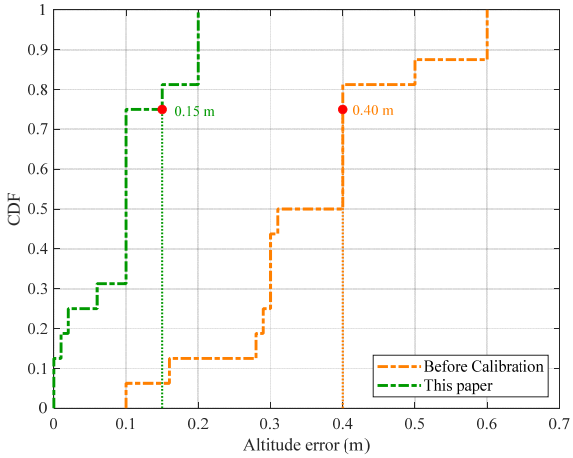

Fig. 13. Altitude error CDF curve.

D. Performance evaluation of EWHT-AIB

To comprehensively assess the overall effectiveness of the proposed EWHT-AIB framework, we conducted comparative experiments against three state-of-the-art PDR-based 3D indoor localization methods: 3D-LBMS, Improved 3-D PDR, and R-AFNIO. The experimental route is shown in Fig. 11, and the final positioning accuracies are summarized in TABLE V.

As presented in TABLE V, the EWHT-AIB framework achieves a 3D localization error of only 2.61 m, significantly outperforming the benchmark methods, whose errors range from 7.55 m to 14.14 m. This performance improvement can be directly attributed to the core design components of EWHT-AIB: the bias-weighted array IMU fusion, the barometric calibration based on nonlinear fitting, and the motion-constrained pose update mechanism.

To further clarify the system's technical advantages, we summarize the key innovations as follows:

Array IMU fusion: Effectively suppresses sensor noise and enhances motion estimation accuracy compared to single-IMU approaches.

Multi-point barometer calibration: Compensates for drift and environmental bias, improving vertical positioning accuracy.

Motion-constrained pose updating: Increases robustness in mixed gait scenarios through QEKF-based filtering and gait-aware corrections.

Additional details of the system structure, fusion strategies, and performance metrics are provided in TABLE VI.

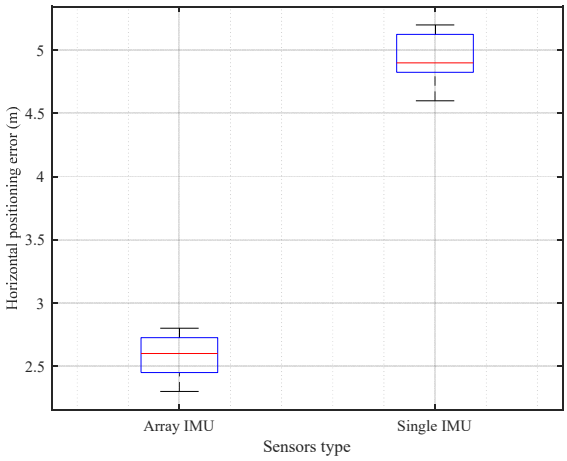

Fig. 14. Comparison of horizontal positioning error bars for different IMU.

TABLE IV
ERROR TABLE OF POSITIONING EXPERIMENTS

Test ID	Horizontal error (m)	Altitude error (m)
1	2.51	0.15
2	2.63	0.14
3	2.85	0.18
4	2.71	0.13
5	2.34	0.15
Mean	**2.61**	**0.15**

TABLE VI
COMPARISON OF DIFFERENT POSITIONING SYSTEMS

System Type	Features	Advantages	Limitations
Single IMU	Low-cost MEMS IMU	Low cost, simple structure	Large drift, poor dynamic accuracy
Array IMU	Multi-IMU fusion	Higher accuracy, noise reduction	Complex hardware, higher power
Barometer	Relative altitude output	Low cost, Floor-level resolution	Easily disturbed, no horizontal positioning
EWHT-AIB	Array IMU + Barometer + Motion constraints	High 3D accuracy, robust	Slightly complex system

TABLE V
ERROR COMPARISON WITH DIFFERENT METHODS

Methods	3D position error (m)
EWHT-AIB	**2.61**
3D-LBMS [35]	7.55
Improved 3-D PDR [36]	10.90
R-AFNIO [37]	14.14

IV. CONCLUSION

To enable high-precision indoor 3D pedestrian positioning, it is crucial to enhance IMU data quality, calibrate barometer deterministic errors, and enforce strict motion constraints. To this end, this paper presents an Enhanced Waist-mounted Human Tracking framework based on an IMU array and barometer (EWHT-AIB). First, a weighted fusion algorithm is introduced to integrate IMU array data, reducing sensor noise and long-term drift using bias instability coefficients from Allan variance analysis. Second, a nonlinear fitting-based barometer calibration method is proposed to suppress deterministic errors and compensate for output nonlinearities, thereby improving relative altitude estimation. Finally, a position-attitude update algorithm based on motion constraints is developed to fuse the IMU and barometer data, enabling accurate and robust 3D indoor localization.

To validate the effectiveness of the proposed algorithm, experimental tests were conducted in a typical indoor environment covering approximately 1000 meters. The results demonstrate that EWHT-AIB achieves a horizontal positioning accuracy of 2.61 m and an altitude positioning accuracy of 0.15 m at the 75th percentile, indicating reliable performance in both horizontal and vertical dimensions.

Despite these promising results, the proposed algorithm has some limitations. First, the calibration of the IMU array currently depends on a high-precision turntable, which may limit its practical deployment and scalability in real-world applications. Second, the pedestrian step length estimation algorithm relies on pre-calibrated parameters, which may reduce adaptability to individual walking styles, speed variations, and different gait patterns. These factors could potentially affect positioning accuracy under diverse scenarios.

To address these limitations, future work will focus on developing a more comprehensive and flexible positioning framework. Specifically, we plan to investigate device calibration techniques that require minimal hardware support or can be conducted using common motion patterns, thereby enhancing practicality and ease of deployment. Furthermore, we aim to explore adaptive step length estimation algorithms leveraging deep learning and data-driven approaches to improve robustness across different users and walking conditions. Additional efforts will be made to validate the proposed system under more complex and varied indoor environments, ensuring its effectiveness and generalizability in real-world applications.

REFERENCES

[1] J. Wang, C. Shi, F. Zheng, et al., "Multi-frequency smartphone positioning performance evaluation: insights into A-GNSS PPP-B2b services and beyond," *Satell. Navig.*, vol. 5, no. 25, 2024.
[2] D. Weng, W. Chen, M. Ding, et al., "Sidewalk matching: a smartphone-based GNSS positioning technique for pedestrians in urban canyons," *Satell. Navig.*, vol. 6, no. 1, p. 4, 2025.
[3] Y. Yu, R. Chen, W. Shi, and L. Chen, "Precise 3D indoor localization and trajectory optimization based on sparse Wi-Fi FTM anchors and built-in sensors," *IEEE Trans. Veh. Technol.*, vol. 71, no. 4, pp. 4042–4056, Apr. 2022.
[4] F. J. Aranda, F. Parralejo, F. J. Álvarez, and J. A. Paredes, "Performance analysis of fingerprinting indoor positioning methods with BLE," *Expert Syst. Appl.*, vol. 202, p. 117095, Apr. 2022.
[5] Z. Yin, X. Jiang, Z. Yang, N. Zhao, and Y. Chen, "WUB-IP: A high-precision UWB positioning scheme for indoor multi-user applications," *IEEE Syst. J.*, vol. 13, no. 1, pp. 279–288, Mar. 2019.
[6] A. A. N. Shirehjini and S. Shirmohammadi, "Improving accuracy and robustness in HF-RFID-based indoor positioning with Kalman filtering and Tukey smoothing," *IEEE Trans. Instrum. Meas.*, vol. 69, no. 11, pp. 9190–9202, Nov. 2020.
[7] Y. Wu, J. Lin, H. Chen, and H. Lan, "A transformer-based double-order RFID indoor positioning system," *Expert Syst. Appl.*, vol. 271, no. 4, p. 126530, May 2025.
[8] S. Bai, W. Wen, D. Su, and L.-T. Hsu, "Graph-Based Indoor 3D Pedestrian Location Tracking With Inertial-Only Perception," *IEEE Trans. Mob. Comput.*, vol. 24, no. 5, pp. 4481–4495, May 2025
[9] J. Huang, M. Zou, S. Wang, Y. Chen, X. Liu, H. Peng, and Y. Liu, "Pedestrian Navigation Using Waist-Mounted IMU and RTK," *IEEE Sens. J.*, early access, Jan. 2024.
[10] L. Qi, Y. Yu, Y. Liu, C. Gao, T. Feng, J. Hui, and S. Wang, "A Robust Foot-Mounted Positioning System Based on Dual IMU Data and Ultrasonic Ranging," *IEEE Sens. J.*, vol. 23, no. 4, pp. 4085–4095, Feb. 2023.
[11] J. Kuang, D. Xia, Y. Wang, and X. Niu, "A Shin-Mounted Inertial Navigation System for Pedestrian Walking and Running Gait," *IEEE Sensors J.*, early access, Jan. 15, 2025.
[12] N. Yu, X. Ma, X. Chen, R. Feng, and Y. Wu, "High-Precision Indoor Positioning Method Based on Multi-Feature Fusion of Inertial Sensor

Network," *IEEE Trans. Instrum. Meas.*, vol. 73, Art. no. 8501416, Jan. 2024.
[13]N. Hajati and A. Rezaeizadeh, "A Wearable Pedestrian Localization and Gait Identification System Using Kalman Filtered Inertial Data," *IEEE Trans. Instrum. Meas.*, vol. 70, pp. 1–8, Apr. 2021.
[14]T. T. Pham and Y. S. Suh, "Walking Step Length Estimation Using Waist-Mounted Inertial Sensors With Known Total Walking Distance," *IEEE Access*, vol. 9, pp. 85476–85487, Jun. 2021.
[15]Y. Li, Z. He, Z. Gao, Y. Zhuang, C. Shi, and N. El-Sheimy, "Toward Robust Crowdsourcing-Based Localization: A Fingerprinting Accuracy Indicator Enhanced Wireless/Magnetic/Inertial Integration Approach," *IEEE Internet Things J.*, vol. 6, no. 2, pp. 3585–3600, Apr. 2019.
[16]T. Zhang, M. Yuan, L. Wang, H. Tang, and X. Niu, "A Robust and Efficient IMU Array/GNSS Data Fusion Algorithm," *IEEE Sens. J.*, vol. 24, no. 16, pp. 26278–26289, Aug. 2024.
[17]L. Wang, H. Tang, T. Zhang, and X. Niu, "Improving the Navigation Performance of the MEMS IMU Array by Precise Calibration," *IEEE Sens. J.*, vol. 21, no. 22, pp. 26050–26058, Nov. 2021.
[18]L. Xing, X. Tu, W. Qian, Z. Chen, and Q. Yang, "Performance Enhancement Method for Angular Rate Measurement Based on Redundant MEMS IMUs," *Micromachines*, vol. 10, no. 8, p. 514, Aug. 2019.
[19]L. Xue, B. Yang, X. Yang, D. Yuan, X. Wang, and H. Chang, "A Redundant Fused MIMU Attitude System Algorithm Based on Two-Stage Data Fusion of MEMS Gyro Clusters Array," *Measurement*, vol. 184, p. 109993, 2021.
[20]Q. Guo, M. Xia, D. Yan, J. Wang, C. Shi, Q. Wang, and T. Li, "Motion pattern recognition for indoor pedestrian altitude estimation based on inertial sensor," *IEEE Sens. J.*, vol. 24, no. 6, pp. 8197–8209, 2024.
[21]H. Qin, Z. Niu, L. Cong, and S. Cao, "Height Estimation for Pedestrian Using Nonscenario-Based Motion Mode Classification," *IEEE Trans. Instrum. Meas.*, vol. 73, pp. 1–12, Mar. 2025.
[22]J. Wang, C. Shi, M. Xia, F. Zheng, T. Li, Y. Shan, G. Jing, W. Chen, and T. C. Hsia, "Seamless Indoor–Outdoor Foot-Mounted Inertial Pedestrian Positioning System Enhanced by Smartphone PPP/3-D Map/Barometer," *IEEE Internet Things J.*, vol. 11, no. 7, pp. 13051–13069, Jul. 2024.
[23]Y. Li, Z. Gao, Z. He, P. Zhang, R. Chen, and N. El-Sheimy, "Multi-Sensor Multi-Floor 3D Localization With Robust Floor Detection," *IEEE Access*, vol. 6, pp. 76689–76699, Dec. 2018.
[24]L. Cong, J. Tian, and H. Qin, "A Practical Hybrid Height Estimation Algorithm Based on FM-Aided Motion Mode Recognition," *IEEE Trans. Instrum. Meas.*, vol. 72, no. 1, pp. 1–13, Jan. 2023.
[25]L. Tran, T. Hoang, T. D. Nguyen, H. Kim, and D. Choi, "Multi-Model Long Short-Term Memory Network for Gait Recognition Using Window-Based Data Segment," *IEEE Access*, vol. 9, pp. 23826–23839, 2021.
[26]A. Bhongade, R. Gupta, M. Bhatia, and T. K. Gandhi, "Classification of Gait Phases Using a Shank-Mounted Single IMU Sensor," *IEEE Sens. J.*, vol. 25, no. 4, pp. 1512–1524, Apr. 2025.
[27]H. Al Jlailaty, A. Celik, M. M. Mansour, and A. M. Eltawil, "IMU hand calibration for low-cost MEMS inertial sensors," *IEEE Trans. Instrum. Meas.*, vol. 72, pp. 1–16, 2023.
[28]F. Huang, Z. Wang, L. Xing, and C. Gao, "A MEMS IMU gyroscope calibration method based on deep learning," *IEEE Trans. Instrum. Meas.*, vol. 71, pp. 1–9, 2022.
[29]Y. Che and J. Dong, "A Real-Time, Robust Visual-Inertial Navigation System Tightly Coupled With GNSS and Barometer," *IEEE Sens. Lett.*, vol. 8, no. 99, pp. 1–4, June 2024.
[30]Y. Yu, R. Chen, L. Chen, W. Li, Y. Wu, and H. Zhou, "Autonomous 3D Indoor Localization Based on Crowdsourced Wi-Fi Fingerprinting and MEMS Sensors," *IEEE Sens. J.*, vol. 22, no. 6, pp. 5248–5259, Mar. 2022.
[31]Y. Sun, X. Xu, X. Tian, L. Zhou, and Y. Li, "A quaternion-based sensor fusion approach using orthogonal observations from 9D inertial and magnetic information," *Inf. Fusion*, vol. 90, pp. 138–147, 2023.
[32]L. Qian, X. Lin, X. Niu, Q. Huang, L. Li, G. Guo, Z. Wang, and R. Chen, "Avnet: learning attitude and velocity for vehicular dead reckoning using smartphone by adapting an invariant EKF," *Satell. Navig.*, vol. 6, art. no. 15, 2025.
[33]F. Lin, S. Wang, Y. Chen, M. Zou, H. Peng, and Y. Liu, "Vehicle integrated navigation IMU mounting angles estimation method based on nonlinear optimization," *Meas. Sci. Technol.*, vol. 35, no. 3, p. 036304, Mar. 2023.
[34]Y. Hu, Y. Liu, L. Li, H. Peng, F. Lin, and Y. Chen, "Foot-mounted inertial navigation algorithm based on dynamic threshold gait detection and adaptive step length estimation," *Meas. Sci. Technol.*, vol. 36, no. 4, Art. no. 046307, Apr. 2025.
[35]Y. Yu, R. Chen, L. Chen, X. Zheng, D. Wu, W. Li, and Y. Wu, "A Novel 3-D Indoor Localization Algorithm Based on BLE and Multiple Sensors," *IEEE Internet Things J.*, vol. 8, no. 11, pp. 9359–9372, Feb. 2021.
[36]C. Li, S. Yu, X. Dong, D. Yu, and J. Xiao, "Improved 3D PDR: Optimized Motion Pattern Recognition and Adaptive Step Length Estimation," *IEEE Sens. J.*, vol. 25, no. 5, pp. 9152–9166, Mar. 2025.
[37]B. Yang, X. Wang, F. Huang, X. Cao, and Z. Zhang, "R-AFNIO: Redundant IMU fusion with attention mechanism for neural inertial odometry," *Expert Syst. Appl.*, vol. 265, Art. no. 125894, Mar. 2025.

Feifan Lin received the M.S. degree from Chongqing University of Posts and Telecommunications, Chongqing, China, in 2024. He is currently pursuing the Ph.D. degree with the School of Instrumentation and Optoelectronic Engineering, Beihang University, Beijing.
His research interests include inertial navigation, and integrated navigation.

Qingzhong Cai (Senior Member, IEEE) received the Ph.D. degree in optical engineering from Beihang University, Beijing, China, in 2014.
He is currently an Associate Professor with the School of Instrumentation and Optoelectronic Engineering, Beihang University.
His current research interests include inertial navigation, integrated navigation, and cooperative navigation.

Yue Yu received dual Ph.D. degrees in both Wuhan University and The Hong Kong Polytechnic University in 2021 and 2022, respectively. is currently a Research Assistant Professor in the Department of Land surveying and Geo-Informatics at the Hong Kong Polytechnic University.
His research interests include Urban Informatics, Seamless Positioning and Navigation, Mobile Mapping, and Geo-spatial Data Analytics.

Huizheng Yuan received the M.S. degree in instruments science and technology from Beihang University, Beijing, China, in 2011.
He is currently an Associate Professor with the School of Mechanical Engineering, Hubei University of Technology.
His current research interests include inertial navigation, and integrated navigation.